

# On the impulse response for swept boundary-layer flows

By R. J. LINGWOOD

Department of Engineering, University of Cambridge, Trumpington Street,  
Cambridge CB2 1PZ, UK

(Received 25 March 1996 and in revised form 11 April 1997)

Swept-wedge flows are used to study the effects of pressure gradient and flow angle on the stability of three-dimensional laminar boundary layers. It is shown that the flow is absolutely unstable in the chordwise direction, i.e. disturbances grow in time at every chordwise location, for certain parameter combinations. However, laminar–turbulent transition may still be a convective process.

---

## 1. Introduction

This paper analyses the linear stability of a family of three-dimensional boundary layers. This study was prompted by the recent discovery by Lingwood (1995, 1996, 1997*a*, *b*) of radial absolute instability of the rotating-disk boundary-layer flow and of related rotating flows such as the Ekman and Bödewadt layers. In those papers it was proposed that this instability mechanism may promote the onset of nonlinearity and laminar–turbulent transition and, because of the similarity between the laminar velocity profiles in the rotating-disk and swept-wing boundary layers, that the same mechanism may exist for swept-wing flows. The rotating-disk boundary-layer flow is often used as a model for the flow over a swept wing because of the similarity of the velocity profiles and because both flows are susceptible to crossflow instability. However, to study more fully the influence of three-dimensionality of the mean boundary-layer flow, it is necessary to have a family of boundary layers in which the magnitude of the inflectional crossflow component can be varied in a systematic way. Here, infinite swept-wedge flows, first introduced by Cooke (1950), are used. For these so-called Falkner–Skan–Cooke boundary-layer flows, it is possible to simulate simple planar three-dimensional boundary layers by varying the pressure-gradient parameter and the ratio of the spanwise to chordwise potential velocities, i.e. the flow angle.

The sweep of a wing affects transition from laminar to turbulent flow in two main ways. First, transition in the attachment-line boundary layer will be discussed. The attachment line is the projection of the dividing stream surface at the leading edge onto the surface of the body and, because for zero sweep it coincides with the locus of two-dimensional stagnation points, it is often called the stagnation line. Note, however, that for non-zero sweep there is a non-zero spanwise velocity along the stagnation line. The transition characteristics of the swept attachment-line flow were first investigated experimentally; see Pfenninger (1977). The small-amplitude stability problem was considered by Gaster (1967). Through experimental studies (e.g. Poll 1979) it was found that, in the absence of large boundary-layer tripping devices, transition of the attachment-line flow resulted from the growth of disturbances, which are excited by free-stream turbulence, in the boundary layer. The disturbances are

convected along the leading edge until the amplitudes are sufficiently large to cause nonlinear breakdown to turbulence. If the attachment-line flow, however, is subjected to large disturbances, for example from the junction of the wing and fuselage or from boundary-layer fences, the flow undergoes premature transition. Second, assuming that there is no premature transition of the attachment-line boundary layer and that it is laminar and stable to small-amplitude free-stream disturbances, then close to the attachment line the potential flow streamlines are highly curved (in planes parallel to the surface of the body) due to the favourable pressure gradient exerted there. Associated with streamline curvature, due to either favourable or adverse pressure gradients, is a pressure gradient that acts in the direction normal to the streamlines, which introduces a secondary crossflow within the boundary layer. The crossflow profile is inflectional and is therefore inviscidly unstable. Crossflow instability often results in the formation of vortices that are fixed relative to the surface of the body; see Gray (1952) and Gregory, Stuart & Walker (1955) for evidence of this on swept wings and on a rotating disk, respectively. These vortices are excited by surface roughness elements. As well as the stationary vortices, travelling crossflow disturbances and viscous streamwise disturbances are also possible. The role that these instability waves play in the transition process of a swept boundary layer that is stable at the attachment line is not fully understood, but visualizations of these flows, which show the fixed vortices rather than any travelling disturbances, indicate that transition is characterized by a jagged chordwise front.

Favourable pressure gradients in the region close to the attachment line on swept wings lead to the growth of inviscid crossflow disturbances, but have a stabilizing effect on Tollmien–Schlichting waves (the result of the viscous instability of the streamwise profiles). Whereas adverse pressure gradients destabilize Tollmien–Schlichting waves. Poll (1985) found that transition in his swept-cylinder experiments was preceded by a high-frequency secondary instability of the stationary crossflow vortices. This suggests that the level of surface roughness was sufficiently large to excite large-amplitude stationary crossflow vortices that modified the mean velocity profiles and introduced a secondary instability of these, rather than the original, profiles. However, from a study of the effects of free-stream turbulence levels, Müller & Bippes (1988) concluded that travelling, and not stationary waves, play the major role in transition. Clearly, depending on the conditions to which the swept flow is subjected, there are different routes to transition.

In this paper, the stability of the theoretical mean velocity profiles is studied, i.e. no account is taken of mean-flow distortions, due to primary instability modes that can lead to secondary instability. Travelling waves (with non-zero frequency) are considered as well as stationary waves. The analysis makes use of the parallel-flow approximation and, therefore, is restricted to the local stability characteristics of the flow. It will be shown that the boundary layer becomes locally absolutely unstable in the chordwise direction for certain Reynolds numbers, pressure gradients and flow angles. However, no simultaneous (or otherwise) spanwise absolute instability could be found, so even disturbances with a chordwise absolute instability continue to convect in the spanwise direction. Note that for a true absolute instability, i.e. in the chordwise and spanwise directions simultaneously, it is necessary to have simultaneous pinching in the respective wavenumber planes; see Bers (1975) and Brevdo (1991). The terminology (*chordwise*) *absolute instability* will be used throughout the paper despite continued convection in the spanwise direction. The physical implications of the chordwise absolute instability seem more limited than the radial absolute instability of the rotating-disk boundary layer. The partially closed nature of the latter flow

means that, although the absolute instability is unidirectional, the disturbances are constrained to convect round circular paths as they grow in time, leading to increasing amplitudes at fixed radial positions. The swept-wing flow, however, is a fully open flow and unidirectional absolute instability does not lead to self-contamination of this sort and, therefore, may not be as important for the transition process. Nevertheless, the results provide useful information on the propagation of wave packets in swept boundary-layer flows.

The structure of the paper is as follows. In §2 there is a description of the problem and in §3 the results are presented and discussed. The conclusions are given in §4.

## 2. Formulation of the problem

The incompressible flow past an infinite swept wedge at zero angle of attack outside the viscous boundary layer is the Falkner–Skan–Cooke potential flow (Cooke 1950). The flow can be represented in the chordwise direction (normal to the leading edge),  $U_{c\infty}^*$ , and the spanwise (parallel to the leading edge) direction,  $V_{s\infty}^*$ , by the following:

$$U_{c\infty}^* = C^*(x_c^*)^m, \quad V_{s\infty}^* = \text{constant}. \quad (2.1)$$

Here, the asterisks indicate dimensional quantities, the subscripts  $c$  and  $s$  indicate the chordwise and spanwise directions, respectively,  $x_c^*$  is the coordinate in the chordwise direction and  $C^*$  is a constant. The wedge angle is  $\beta_H\pi/2$ , where  $\beta_H$  is the usual two-dimensional (Falkner–Skan) pressure-gradient parameter, known as the Hartree parameter, and  $\beta_H = 2m/(m+1)$ . For this free-stream flow there is a similarity solution of the boundary-layer equations, in which the variables are functions of the wall-normal similarity variable  $z = z^*/l^*$  only, where  $l^* = [(m+1)U_{c\infty}^*/(2\nu^*x_c^*)]^{-1/2}$  and  $\nu^*$  is the kinematic viscosity. Rosenhead (1963), for example, shows that the boundary-layer equations reduce to

$$f''' + ff'' + \beta_H(1 - f'^2) = 0, \quad (2.2)$$

$$g'' + fg' = 0, \quad (2.3)$$

where  $f(z) = U_c^*/U_{c\infty}^*$ ,  $g(z) = V_s^*/V_{s\infty}^*$  and the primes indicate differentiation with respect to  $z$ . The boundary conditions are

$$f(0) = f'(0) = g(0) = 0, \quad f'(\infty) = g(\infty) = 1. \quad (2.4)$$

A double-precision fourth-order Runge–Kutta integrator and a Newton–Raphson searching method were used to solve (2.2) and (2.3).

The streamwise and crossflow velocity profiles can be constructed from  $f'(z)$  and  $g(z)$ . There is no undisturbed free-stream for Falkner–Skan–Cooke flows, but if such a direction is assumed then a sweep angle  $\psi$  can be defined relative to it. The local potential flow,  $U_\infty^* = (U_{c\infty}^{*2} + V_{s\infty}^{*2})^{1/2}$ , is at an angle  $\psi_l$  to the undisturbed direction and the local potential flow defines the streamwise direction,  $x$ , to which the crossflow direction,  $y$ , is normal. The angle between the streamwise direction and the chordwise direction is the flow angle  $\theta$ , where

$$\theta = \tan^{-1} \left( \frac{V_{s\infty}^*}{U_{c\infty}^*} \right). \quad (2.5)$$

Using the local potential velocity  $U_\infty^*$  as the reference velocity, the dimensionless

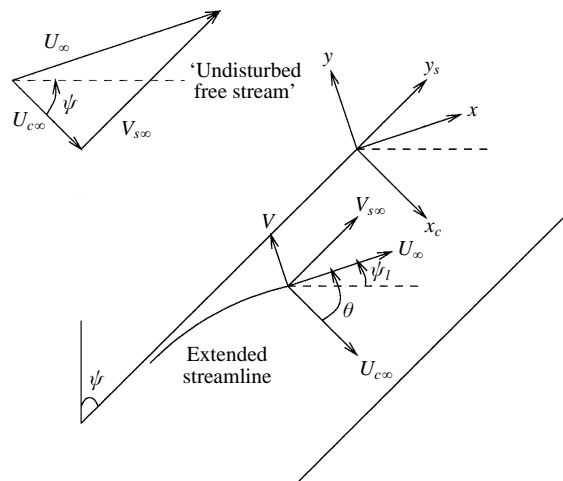


FIGURE 1. Sketch of the flow geometry. The local potential flow is shown displaced to the top left-hand corner.

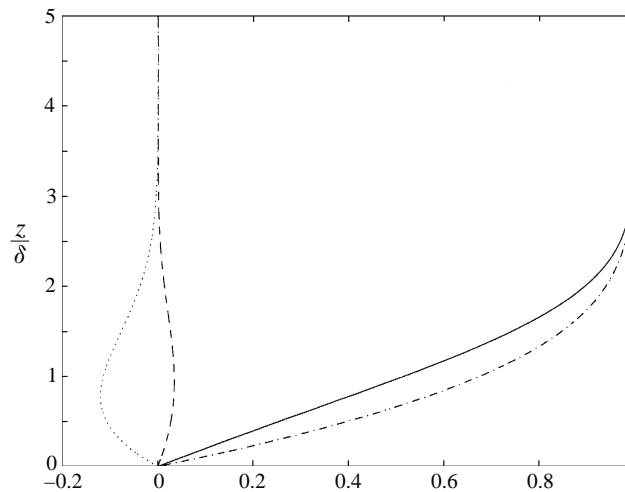


FIGURE 2. Streamwise (—) and crossflow (----) velocity profiles for  $\theta = 45^\circ$  and  $\beta_H = -0.1$ , and  $U$  (-·-·-) and  $V$  (·····) velocity profiles for  $\theta = 45^\circ$  and  $\beta_H = 1.0$ .

streamwise and crossflow velocity components are

$$U(z) = f'(z) \cos^2 \theta + g(z) \sin^2 \theta, \quad (2.6)$$

$$V(z) = (g(z) - f'(z)) \cos \theta \sin \theta. \quad (2.7)$$

Figure 1 shows the appropriate flow geometry, in which the  $z$ -direction is out of the plane. Figure 2 shows the mean velocity profiles in the streamwise direction ( $x$ ) and crossflow direction ( $y$ ) for  $\theta = 45^\circ$  and  $\beta_H = -0.1$  and  $\beta_H = 1.0$ . The profiles are plotted against  $z/\delta$ , where  $\delta = \delta^*/l^*$  is the non-dimensional displacement thickness based on the streamwise velocity component. For zero pressure gradient, i.e.  $\beta_H = m = 0$ , and any  $\theta$  the flow reduces to the Blasius flow and  $\delta$  takes the familiar value 1.2167. Note that for fixed  $\beta_H$  all the crossflow profiles have the same shape;

only the magnitude varies with  $\theta$ . However, the streamwise profiles change shape with  $\theta$ .

Physical quantities are non-dimensionalized using the length, time, velocity and pressure scales  $\delta^*$ ,  $\delta^*/U_\infty^*$ ,  $U_\infty^*$  and  $\rho^*U_\infty^{*2}$  (where  $\rho^*$  is the fluid density), respectively. The Reynolds number is then given by

$$R_\delta = \frac{R_c}{\cos \theta} = \frac{R_s}{\sin \theta} = \frac{\delta^* U_\infty^*}{\nu^*}, \quad (2.8)$$

where  $R_c$  and  $R_s$  are chordwise and spanwise Reynolds numbers, respectively.

The parallel-flow assumption is made and linearized perturbation quantities of the form  $w(x, y, z, t) = \hat{w}(z)e^{i(\alpha x + \beta y - \omega t)}$  (where  $\alpha$ ,  $\beta$  and  $\omega$  are the crossflow wavenumber, streamwise wavenumber and perturbation frequency, respectively, and  $w$  is the perturbation velocity in the wall-normal direction) then satisfy a system of six first-order ordinary-differential equations that are equivalent to the fourth-order Orr–Sommerfeld equation

$$(\alpha U + \beta V - \omega)(\hat{w}'' - \gamma^2 \hat{w}) - (\alpha U'' + \beta V'')\hat{w} + \frac{i}{R_\delta}(\hat{w}'''' - 2\gamma^2 \hat{w}'' + \gamma^4 \hat{w}) = 0, \quad (2.9)$$

and the coupled second-order Squire-mode equation (Squire 1933)

$$(\alpha U + \beta V - \omega)\eta - i(\alpha V' + \beta U')\hat{w} + \frac{i}{R_\delta}(\eta'' - \gamma^2 \eta) = 0. \quad (2.10)$$

Here  $\hat{w}$  is the vertical component of the three-dimensional spectral velocity perturbation  $\hat{\mathbf{u}} = (\hat{u}, \hat{v}, \hat{w})$ ,  $\eta = \alpha \hat{v} - \beta \hat{u}$  is the vertical component of vorticity,  $\gamma^2 = \alpha^2 + \beta^2$  and the primes denote differentiation with respect to  $z$ . The equations can also be written in terms of the chordwise and spanwise quantities. For example, the Orr–Sommerfeld equation (2.9) can be written

$$(\alpha_c U_c + \beta_s V_s - \omega)(\hat{w}'' - \gamma^2 \hat{w}) - (\alpha_c U_c'' + \beta_s V_s'')\hat{w} + \frac{i}{R_\delta}(\hat{w}'''' - 2\gamma^2 \hat{w}'' + \gamma^4 \hat{w}) = 0, \quad (2.11)$$

where  $\gamma^2 = \alpha^2 + \beta^2 = \alpha_c^2 + \beta_s^2$  and  $\hat{w}(z)e^{i(\alpha x + \beta y - \omega t)} = \hat{w}(z)e^{i(\alpha_c x_c + \beta_s y_s - \omega t)}$ .

To distinguish between a convectively and an absolutely unstable response, consider an impulsive point forcing, such that the vertical velocity at  $z = 0$  is given by

$$w(0; x_c, y_s, t) = \delta(x_c - x_{c0})\delta(y_s - y_{s0})\delta(t), \quad (2.12)$$

where  $\delta(x_c - x_{c0})$ ,  $\delta(y_s - y_{s0})$  and  $\delta(t)$  are the Dirac delta functions at  $x_{c0}$ ,  $y_{s0}$  and  $t = 0$ , respectively. The additional boundary conditions at  $z = 0$ , given by the no-slip condition, are

$$u(0; x_c, y_s, t) = v(0; x_c, y_s, t) = 0, \quad (2.13)$$

and as  $z \rightarrow \infty$  it is required that all perturbations decay.

The problem reduces to solving a Green's function of the form

$$w(z; x_c, y_s, t) = \frac{1}{(2\pi)^3} \int_B \int_A \int_F \frac{\Phi(z; \alpha_c, \beta_s, \omega; R_\delta)}{\Delta_0(\alpha_c, \beta_s, \omega; R_\delta)} e^{i(\alpha_c(x_c - x_{c0}) + \beta_s(y_s - y_{s0}) - \omega t)} d\omega d\alpha_c d\beta_s, \quad (2.14)$$

where  $\Phi$  is a function of  $z$  formed from a combination of the independent solution vectors of the governing ordinary-differential equations (see Lingwood 1997c),  $\Delta_0 = 0$  is the dispersion relation, which is satisfied by the discrete eigenvalues

of the homogeneous problem (the unforced case) and  $A$ ,  $B$  and  $F$  are inversion contours in the  $\alpha_c$ -,  $\beta_s$ - and  $\omega$ -planes, respectively. The discrete eigenvalues (found using a double-precision fixed-step-size fourth-order Runge–Kutta integrator, a Newton–Raphson linear search procedure and Gram–Schmidt orthonormalization) provide a mapping between the complex wavenumber planes and the frequency plane, e.g. zeros of the dispersion relation in the  $\alpha_c$ -plane are given by

$$\alpha_c = \alpha_{cj}(\omega, \beta_s; R_\delta), \quad j = 1, \dots, M, \quad (2.15)$$

where  $M$  is the number of discrete modes in the  $\alpha_c$ -plane. Note that the governing equations have a symmetry property, whereby  $\alpha_{cj}(\omega, \beta_s; R_\delta) \mapsto -\alpha_{cj}^\times(-\omega^\times, -\beta_s^\times; R_\delta)$  and  $\omega_j(\alpha_c, \beta_s; R_\delta) \mapsto -\omega_j^\times(-\alpha_c^\times, -\beta_s^\times; R_\delta)$ , where  $\times$  indicates the complex conjugate. Thus, for example, trajectories of the dispersion relation given by (2.15) for  $\omega_r < 0$  and  $\beta_{sr} < 0$  (henceforth, the subscripts  $r$  and  $i$  will be used for real and imaginary parts, respectively) are symmetric with respect to the imaginary  $\alpha_c$ -axis to those for  $\omega_r > 0$  and  $\beta_{sr} > 0$ .

The inversion contours must lie in regions of analyticity in the respective complex planes. Therefore, the contours must avoid continuous and discrete singularities. If the inversion contours are incorrectly taken through regions of non-analyticity, the inversions can still be formally carried out but, as well as being non-causal, the solution may not converge to a solution of the original problem. In both the  $\alpha_c$ - and  $\beta_s$ -planes there is a strip of analyticity of non-zero width, centred on the respective real axes. Note that the  $\omega$ -dependent hyperbolic branch cuts (Ashpis & Reshotko 1990; Lingwood 1997c) in the  $\alpha_c$ - and  $\beta_s$ -planes always lie in the distinct halves of those planes. Taking the  $A$ - and  $B$ -contours along the real  $\alpha_c$ - and  $\beta_s$ -axes, respectively, gives purely temporal branches of the dispersion relation in the  $\omega$ -plane. The region of analyticity in the  $\omega$ -plane lies above, and includes, the horizontal  $F$ -contour that must lie above all the discrete singularities and branch cuts given by the  $A$ - and  $B$ -contours for zero response at  $t < 0$ . The branch cuts in the  $\omega$ -plane always lie below the real  $\omega$ -axis when  $\alpha_c$  and  $\beta_s$  are real. The  $F$ -contour produces branches in the  $\alpha_c$ - and  $\beta_s$ -planes that are not purely spatial since they have complex  $\omega$ , with positive  $\omega_i$ . Nonetheless, any branch of the dispersion relation given by a predetermined  $\omega$ -distribution will be referred to as a spatial branch; similarly, any branch that lies in the  $\omega$ -plane and is given by predetermined  $\alpha_c$ - and  $\beta_s$ -distributions, which may be complex, will be called a temporal branch. With  $\omega_i$  above any singularities in the  $\omega$ -plane, the spatial branches do not cross the real  $\alpha_c$ - and  $\beta_s$ -axes and they correspond to spatially damped eigenvalue solutions. It follows that any branch lying in the upper-half  $\alpha_c$ -plane ( $\beta_s$ -plane) leads to a response in the physical region  $x_c > x_{c0}$  ( $y_s > y_{s0}$ ), while any branch lying in the lower-half  $\alpha_c$ -plane ( $\beta_s$ -plane) corresponds to the region  $x_c < x_{c0}$  ( $y_s < y_{s0}$ ). The above choice of contours ensures convergence of the transforms and satisfies causality.

The integrals given by (2.14) give the exact solution for the axial perturbation velocity  $w$ , when the boundary-layer flow is impulsively disturbed in the way described by (2.12). The solution can be evaluated by direct numerical integration or, alternatively, by asymptotic methods, in which only dominant terms are considered. Here the method of steepest descent, in which  $(x_c - x_{c0})/t$  and  $(y_s - y_{s0})/t$  are kept constant as  $t \rightarrow \infty$ , is used to predict the time-asymptotic impulse response. The discrete response is sufficient to determine the nature of the instability so, neglecting the continuous spectra (the branch-cut contributions), the  $\omega$ -integral is performed first by closing the

$F$ -contour with semicircles at infinity and using the residue theorem

$$w(z; x, y, t) = \frac{H(t)}{(2\pi)^2 i} \int_B \int_A \sum_{j=1}^M \Theta_j(z; \alpha_c, \beta_s) e^{-i\psi_j(\alpha_c, \beta_s)t} d\alpha_c d\beta_s, \quad (2.16)$$

where

$$\Theta_j(z; \alpha_c, \beta_s) = \frac{\Phi(z; \alpha_c, \beta_s, \omega_j(\alpha_c, \beta_s); R_\delta)}{\partial \Delta_0(\alpha_c, \beta_s, \omega_j(\alpha_c, \beta_s); R_\delta) / \partial \omega_j}, \quad (2.17)$$

and

$$\psi_j(\alpha_c, \beta_s) = - \left( \frac{\alpha_c(x_c - x_{c0})}{t} + \frac{\beta_s(y_s - y_{s0})}{t} - \omega_j(\alpha_c, \beta_s) \right). \quad (2.18)$$

Here,  $\psi_j$  is the complex phase function,  $M$  is the number of discrete first-order poles  $\omega_j(\alpha_c, \beta_s)$  of the  $\omega$ -integrand and  $H(t)$  is the unit-step function in time. In general, the function  $\Theta_j(z; \alpha_c, \beta_s)$  has branch-pole singularities (due to poles coalescing) at branch points of  $\omega(\alpha_c, \beta_s)$ , where  $\partial \Delta_0 / \partial \omega = 0$  and  $\partial \omega / \partial \alpha_c = \partial \omega / \partial \beta_s = \infty$ . However, the sum over all  $j$  does not have any singularities; the summation  $\sum_{j=1}^M \Theta_j(z; \alpha_c, \beta_s)$  is an entire function. This must be so, because the branch points of  $\omega(\alpha_c, \beta_s)$  are just multiple roots of  $\omega$  for some  $\alpha_c$  and  $\beta_s$ , all roots are included in the residue evaluation, and the terms that individually have a singularity cancel. (Coalescing residues do not cancel if they pinch the integration contour, but it is not possible for multiple roots of  $\omega$  to pinch the  $F$ -contour because there are no discrete poles above the  $F$ -contour from causality arguments.)

The method of steepest descent is used to evaluate the large-time solutions of the remaining  $\alpha_c$ - and  $\beta_s$ -integrals along rays of constant  $(x_c - x_{c0})/t$  and  $(y_s - y_{s0})/t$ , respectively. Dominant contributions are given by the stationary points of  $\psi_j$ , which can be shown to be always saddle points. So, if the end points of each steepest-descent integration are separated by, say, a single saddle point of  $\psi_j$ , the  $A$ - and  $B$ -contours (along the real  $\alpha_c$ - and  $\beta_s$ -axes, respectively) are deformed onto steepest-descent paths that pass through the saddle points  $\alpha_c^*$  and  $\beta_s^*$  (at which  $\partial \psi_j / \partial \alpha_c = \partial \psi_j / \partial \beta_s = 0$ , and  $\star$  denotes the saddle point), where  $\omega_j^* \equiv \omega_j(\alpha_c^*, \beta_s^*)$  and  $\psi_j^* \equiv \psi_j(\alpha_c^*, \beta_s^*)$ . A steepest-descent path lies along a line where  $\psi_{ji}$  decreases most rapidly, namely orthogonal to the lines of constant  $\psi_{ji}$ , and is therefore (from the Cauchy–Riemann equations) given by a line of constant  $\psi_{jr}$  through the saddle point. In general, the limits of the integral do not lie on the steepest-descent path, but they can be joined to it within valleys of  $\psi_{ji}$ , i.e. where  $\psi_{ji} < \psi_j^{j\star}$ .

As  $t \rightarrow \infty$  with fixed  $(x_c - x_{c0})/t$  and  $(y_s - y_{s0})/t$ , integration along the steepest-descent paths is dominated by the contribution given by the saddle point of  $\psi_j$ . At these saddle points

$$\left. \frac{\partial \omega_j}{\partial \alpha_c} \right|_{\alpha_c^*, \beta_s^*} = \frac{x_c - x_{c0}}{t} \equiv U^*, \quad \left. \frac{\partial \omega_j}{\partial \beta_s} \right|_{\alpha_c^*, \beta_s^*} = \frac{y_s - y_{s0}}{t} \equiv V^*, \quad (2.19)$$

which are real and therefore

$$\left. \frac{\partial \omega_{ji}}{\partial \alpha_{cr}} \right|_{\alpha_c^*, \beta_s^*} = \left. \frac{\partial \omega_{ji}}{\partial \beta_{sr}} \right|_{\alpha_c^*, \beta_s^*} = 0. \quad (2.20)$$

Assuming that there is a single saddle point of  $\psi_j$  through which the integration contour can be made to pass for each value of  $j$ , and provided  $\partial^2 \omega_j / \partial \alpha_c^2 |_{\alpha_c^*, \beta_s^*}$  is nowhere zero, following standard mathematics textbooks the time-asymptotic impulse

response to (2.16) reduces to

$$w(z; x, y, t) \sim \frac{iH(t)}{2\pi} \sum_{j=1}^M \frac{\Theta_j(z; \alpha_c^*, \beta_s^*) e^{i(\alpha_c^*(x_c - x_{c0}) + \beta_s^*(y_s - y_{s0}) - \omega_j^* t)}}{f_j(\alpha_c^*, \beta_s^*) t}, \quad (2.21)$$

where

$$f_j(\alpha_c^*, \beta_s^*) = \left[ \left( \frac{\partial^2 \omega_j}{\partial \alpha_c \partial \beta_s} \right)^2 - \frac{\partial^2 \omega_j}{\partial \alpha_c^2} \frac{\partial^2 \omega_j}{\partial \beta_s^2} \right]_{|\alpha_c^*, \beta_s^*}^{1/2}, \quad (2.22)$$

and where  $\Theta_j/f_j$  is a function that gives the leading-order term of the asymptotic approximation. In general, it is not possible to deform an integration path through all saddle points. Therefore, it is not sufficient simply to locate saddle points of the complex phase function without examining the global topography of the phase function. However, examination of this problem in Lingwood (1997c) (for a one-dimensional Green's function, i.e. where  $\psi$  is independent of  $\beta_s$  and  $y_s$ ) shows that there is a direct correspondence between Briggs' criterion (Briggs 1964; Bers 1975) and whether the steepest-descent path can pass through the saddle point. Considering a one-dimensional Green's function for a moment, for  $U^* = 0$ ,  $\psi_j^* = \omega_j^*$  and therefore saddle points of the phase function are equally saddle points of the dispersion relation. It is known for this case (e.g. Huerre & Monkewitz 1990) that  $\omega_{ji}^* > 0$  only indicates temporal growth at  $x_c = x_{c0}$ , i.e. absolute instability, if  $\omega_j^*$  is a pinch point of  $\alpha_c^*(\omega_j)$ . The pinching condition is stipulated by Briggs' criterion and requires that the two spatial branches of the dispersion relation that coalesce at  $\alpha_c^*$  originate in distinct halves (upper and lower) of the  $\alpha_c$ -plane when  $\omega_i$  is sufficiently large and positive. Such singularities have become known as pinch points because inherent in Briggs' method is the use of analytic continuation to deflect the inversion contours, and at these singularities the  $A$ -contour becomes pinched between the coalescing spatial branches. A branch-point singularity between two spatial branches that originate in the same half of the  $\alpha_c$ -plane for large positive  $\omega_i$  does not constitute a pinch point (even though  $\partial\omega/\partial\alpha_c = 0$  at such a point) and does not cause an absolute instability. Furthermore, for non-zero values of  $U^*$ , saddle-point contributions are only relevant if the coalescing branches of  $\alpha(\psi)$  originate in distinct half-planes for large positive  $\psi_i$ , i.e. if the branches pinch the steepest-descent path; see Lingwood (1997c). In practice, for the time-asymptotic response (2.21), the summation over  $M$  is limited to the number of unstable modes. The physical solution is given by the real part of (2.21).

As  $U^*$  and  $V^*$  vary, the respective (relevant) saddle points trace paths in the complex  $\alpha_c$ - and  $\beta_s$ -planes; each point being related to a ray in the physical  $(x_c, t)$ - and  $(y_s, t)$ -spaces. Along each ray the response is dominated by the exponential term of (2.21) and has the form of a travelling wave with constant complex values of frequency and streamwise and crossflow wavenumbers. The temporal growth rate along rays is

$$\psi_{ji}^* = \omega_{ji}^* - \frac{\alpha_{ci}^*(x_c - x_{c0})}{t} - \frac{\beta_{si}^*(y_s - y_{s0})}{t}. \quad (2.23)$$

Following the response along given  $U^*$ - and  $V^*$ -rays corresponds to a moving observation position travelling at  $\partial\omega_{jr}/\partial\alpha_{cr}|_{\alpha_c^*, \beta_s^*}$  and  $\partial\omega_{jr}/\partial\beta_{sr}|_{\alpha_c^*, \beta_s^*}$  in the  $x_c$ - and  $y_s$ -directions, respectively. If  $\psi_{ji}^*$  is positive, the disturbance grows in time in that reference frame; if  $\psi_{ji}^*$  is negative, the waves decay in amplitude as they travel and the flow returns to its undisturbed state.

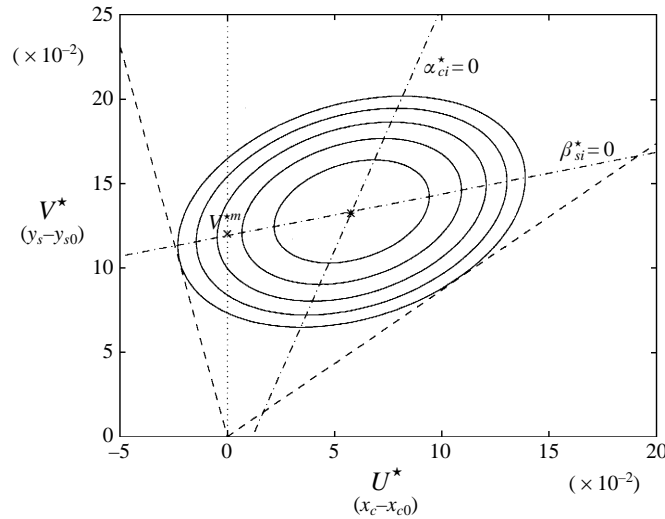


FIGURE 3. Sketch of contours of  $\psi_i^* \geq 0$ , showing chordwise absolute instability. The wedge of growth in  $(x_c, y_s)$ -space as  $t$  varies is denoted by ----.

Figure 3 shows a sketch of contours  $\psi_i^* \geq 0$  (dropping the  $j$  subscript), i.e. rays of  $U^*$  and  $V^*$  where there is zero or positive growth. For the example given in figure 3, the maximum growth has positive  $U^*$  and  $V^*$  and therefore the maximum of the wave packet is convectively unstable. However, the trailing edge of the packet crosses the  $V^*$ -axis, which implies that there is growth in time for  $U^* = 0$  that shall be referred to as an absolute instability in the  $x_c$ -direction, i.e. a chordwise absolute instability. Note that the  $U^*$ -axis and  $V^*$ -axis can be thought of as the  $(x_c - x_{c0})$ -axis and  $(y_s - y_{s0})$ -axis, respectively, in which case the growth-rate contours represent the positions in space where the wave packet is growing at a particular instant in time and the dashed lines indicate the wedge of growth in  $(x_c, y_s)$ -space as  $t$  varies. Differentiating  $\psi_i^*$  with respect to  $U^*$  and  $V^*$  shows that, although in general  $\alpha_{ci}^*$  and  $\beta_{si}^*$  are complex, for any fixed  $U^*$  ( $V^*$ ) the maximum growth rate with respect to  $V^*$  ( $U^*$ ) is given by the saddle point for which  $\beta_{si}^* = 0$  ( $\alpha_{ci}^* = 0$ ). For example, consider the case where  $U^* = 0$  then

$$\psi_i^* = \omega_i^* - \beta_{si}^* V^*, \tag{2.24}$$

and maximizing with respect to  $V^*$  gives

$$\frac{\partial \psi_i^*}{\partial V^*} = \frac{\partial \omega_i^*}{\partial \beta_{si}^*} \frac{\partial \beta_{si}^*}{\partial V^*} - \beta_{si}^* - \frac{\partial \beta_{si}^*}{\partial V^*} V^* = 0. \tag{2.25}$$

Because of the Cauchy–Riemann relations ( $\partial \omega_i^* / \partial \beta_{si}^* = \partial \omega_r^* / \partial \beta_{sr}^* = V^*$ ) the first and third terms cancel, implying that  $\beta_{si}^* = 0$ . The dashed-dotted lines in figure 3 denote lines of  $\alpha_{ci}^* = 0$  and  $\beta_{si}^* = 0$ . Clearly, the maximum in  $\psi_i^*$  is given by the particular saddle points for which both  $\alpha_{ci}^* = 0$  and  $\beta_{si}^* = 0$ , where the lines intersect.

In this study of Falkner–Skan–Cooke boundary layers no true absolute instability (growth in time for fixed  $x_c$  and  $y_s$ ) could be found. Note that for a true absolute instability (i.e. in the chordwise and spanwise directions simultaneously), which would result in the contours of  $\psi_i^* \geq 0$  covering the origin in figure 3, it is necessary to have simultaneous pinching in the respective wavenumber planes; see Bers (1975) and Brevdo (1991). In fact, no spanwise absolute instability (growth in time for fixed  $y_s$ ) was found. However, chordwise absolute instability (where disturbances continue

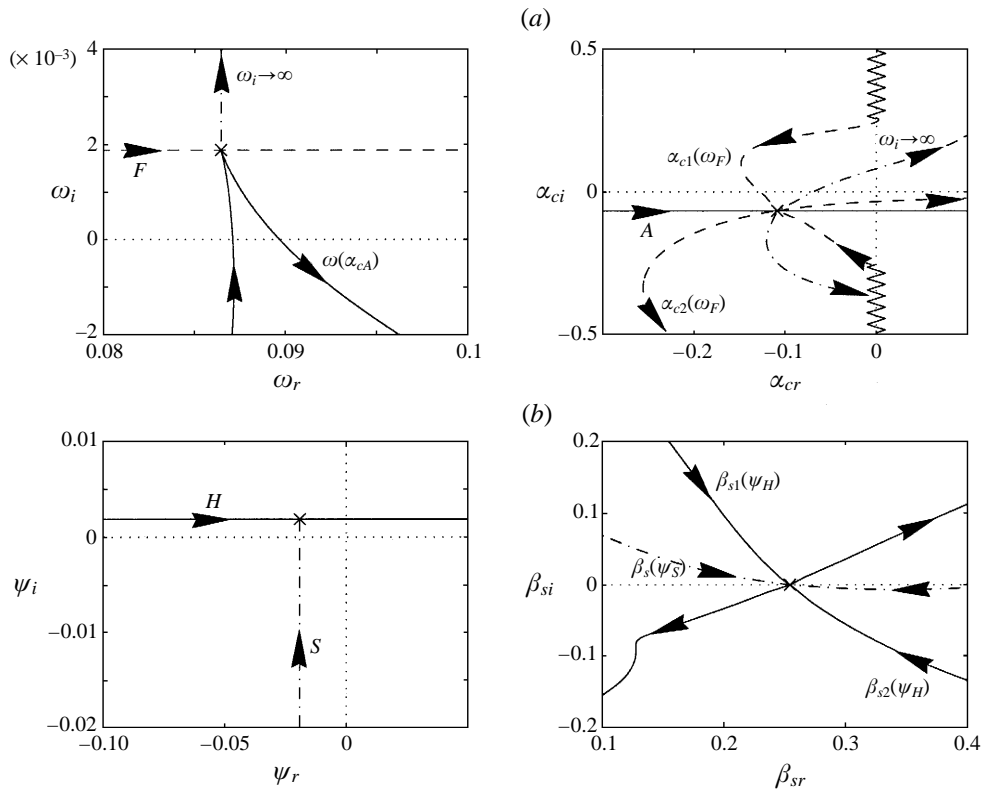


FIGURE 4. (a) Temporal branch in the  $\omega$ -plane (given by the  $A$ -contour) and spatial branches in the  $\alpha_c$ -plane (given by the  $F$ -contour), for  $R_\delta = 1000$ ,  $\beta_H = -0.1$ ,  $\theta \approx 80.9^\circ$  and  $\beta_s = \beta_s^* \approx 0.255$ . Branch cuts in the  $\alpha_c$ -plane are indicated by zigzag lines,  $\omega^*$  and  $\alpha_c^*$  are marked by  $\times$  and the mapping of  $\omega = \omega^* + i\omega_i$ , where  $\omega_i \rightarrow \infty$  is shown in the  $\alpha_c$ -plane ( $-\cdot-\cdot-$ ). (b) Mapping of the steepest-descent path ( $S$ ) from the  $\psi$ -plane to the  $\beta_s$ -plane ( $-\cdot-\cdot-$ ) and the mapping of  $\psi_i = \psi_i^*$  (where  $\psi^*$  is denoted by  $\times$ ) to the  $\beta_s$ -plane ( $---$ );  $R_\delta = 1000$ ,  $\beta_H = -0.1$ ,  $\theta \approx 80.9^\circ$ ,  $\alpha_c = \alpha_c^*$ .

to convect in the spanwise direction but grow in time at fixed  $x_c$ ) was found. In the results that follow, examples of pinch points in the complex  $\alpha_c$ -plane ( $\partial\omega/\partial\alpha_c = 0$ ) for real  $\beta_s$  and  $\partial\omega_i/\partial\beta_{sr} = 0$  will be shown. These points satisfy the saddle-point conditions (2.19) and (2.20) for  $U^* = 0$  and, because  $\beta_{si} = 0$ , for the value  $V^*$  that has the maximum growth:  $V^{*m}$  as shown by  $\times$  in figure 3. These points illustrate chordwise absolute instability.

### 3. Results and discussion

#### 3.1. Non-attachment-line flows

A swept flow with an adverse pressure gradient of  $\beta_H = -0.1$  has been chosen, which corresponds to the flow around an infinite swept expansion corner of  $9^\circ$ , to study the behaviour of a flow for which there is the possibility of both crossflow and streamwise instability at low Reynolds number.

Figure 4(a) shows the complex  $\omega$ - and  $\alpha_c$ -planes with  $\beta_s = \beta_s^* \approx 0.255$ , and figure 4(b) shows the  $\psi$ - and  $\beta_s$ -planes with  $\alpha_c = \alpha_c^* \approx -0.108 - i0.0660$ ;  $R_\delta = 1000$ ,  $\beta_H = -0.1$  and  $\theta \approx 80.9^\circ$ . The zigzag lines in the  $\alpha_c$ -plane represent the imaginary-axis branch cuts that end in branch points at  $\alpha_{ci} = \pm\beta_s^*$  (see Lingwood 1997c). The

dashed line in the  $\omega$ -plane is the analytic continuation of the  $F$ -contour from (2.14) and values of  $\omega$  on this line map to the dashed spatial branches in the  $\alpha_c$ -plane, which are labelled  $\alpha_{c1}(\omega_F)$  and  $\alpha_{c2}(\omega_F)$ . Similarly, the solid line in the  $\alpha_c$ -plane is the analytic continuation of the  $A$ -contour from (2.14) and it maps to the solid temporal branch in the  $\omega$ -plane, which is labelled  $\omega(\alpha_{cA})$ . Figure 4(a) shows the  $A$ -contour being pinched between coalescing spatial branches when the  $F$ -contour is lowered from its original position towards the real  $\omega$ -axis. This process of deforming the  $A$ - and  $F$ -contours is an integral part of Briggs' method of solving for the time-asymptotic impulse response but, as discussed in §2, for a saddle point in the  $\alpha_c$ -plane to contribute to the time-asymptotic impulse response calculated using the method of steepest descent it is necessary for  $\omega^*$  to be a pinch point of  $\alpha_c(\omega)$ . The vertical dashed-dotted line that extend upwards from the branch point at  $\omega^*$  ( $\times$ ) in the  $\omega$ -plane shows the effect of increasing  $\omega_i$  while keeping all other parameters constant at the branch point values. The mapping of the dashed-dotted line into the  $\alpha_c$ -plane results in two lines extending from  $\alpha_c^*$  ( $\times$ ) into distinct halves of the  $\alpha_c$ -plane. Thus, the  $A$ -contour is pinched between two coalescing spatial branches for positive  $\omega_i$ . Figure 4(b) (where lines of one type map to lines of the same type in the neighbouring plane) shows that the mapping into the  $\beta_s$ -plane of the steepest-descent path ( $S$ ) in the  $\psi$ -plane, which by definition has constant  $\psi_r$  and a maximum of  $\psi_i$  at the branch point  $\psi^*$  that maps to the saddle point in the  $\beta_s$ -plane (both marked by  $\times$ ), is pinched by coalescing branches of  $\beta_s(\psi)$ , i.e.  $\psi^*$  is a pinch point of  $\beta_s(\psi)$ , indicating that this saddle point in the  $\beta_s$ -plane contributes to the time-asymptotic impulse response. The line labelled  $H$  in the  $\psi$ -plane, when mapped to the  $\beta_s$ -plane, gives the height of the saddle point and therefore bounds the valleys of  $\psi_i$ , through which the steepest-descent path must pass. Because  $\partial\omega_i/\partial\beta_{sr} = \beta_{si} = 0$  at this pinch point, the saddle-point conditions are satisfied and furthermore this pinch point gives the maximum temporal growth rate over all  $V^*$  for  $U^* = 0$  (and the given  $R_\delta$ ,  $\theta$  and  $\beta_H$ ); see the discussion associated with figure 3. Thus, this pinch point indicates a chordwise absolute instability and  $\partial\omega_r/\partial\beta_{sr}|_{\alpha_c^*,\beta_s^*} \equiv V^{*m} \approx 0.415$  gives the speed of propagation of the maximum of the wave packet in the  $y_s$ -direction for  $x_c = x_{c0}$ . In figure 4(a),  $U^* = 0$  and  $\beta_s = \beta_s^*$  is real and fixed, therefore the  $\omega$ -plane is simply a horizontal translation of the  $\psi$ -plane by an amount given by  $\beta_s^* V^{*m}$  (mappings in the  $\alpha_c$ -plane would be unaffected by this translation), and the  $F$ - and  $H$ -lines have the same imaginary parts. In figure 4(b), where  $\alpha_c = \alpha_c^*$ ,  $U^* = 0$  and  $V^* = V^{*m} \neq 0$ , as  $\psi$  varies so do both  $\beta_s$  and  $\omega$ , and so the  $\omega$ -plane is no longer a simple translation of the  $\psi$ -plane. Note that the cusp in  $\omega(\alpha_{cA})$  at  $\omega^*$  in figure 4(a) is a characteristic of a pinch point. This feature has been used by Kupfer, Bers & Ram (1987) to locate points of absolute instability.

The solid and dotted lines in figure 5 are loci of points on two Riemann sheets of the dispersion relation for which  $\partial\omega/\partial\alpha_c = \omega_i = 0$ , for  $R_\delta = 1000$  and  $\beta_H = -0.1$ . Note that for favourable pressure gradients ( $\beta_H > 0$ )  $\theta = 90^\circ$  at  $x_c = 0$  and  $\theta \rightarrow 0^\circ$  as  $x_c \rightarrow \infty$ ; for adverse pressure gradients ( $\beta_H < 0$ )  $\theta = 0^\circ$  at  $x_c = 0$  and  $\theta \rightarrow 90^\circ$  as  $x_c \rightarrow \infty$ . Therefore for flows with adverse pressure gradients and  $\theta = 90^\circ$ ,  $R_\delta$  must be infinite. Nonetheless, for the moment,  $\theta$  will be regarded as a free parameter. Inside the curves  $\partial\omega/\partial\alpha_c = 0$  (i.e.  $U^* = 0$ ) and  $\omega_i > 0$ , but it is only on the dashed and dashed-dotted lines that  $\partial\omega_i/\partial\beta_{sr} = 0$ ; only on these lines are the saddle-point conditions (2.19) and (2.20) satisfied fully. These lines intersect at  $\beta_{sr} \approx 0.255$  and  $\theta \approx 80.9^\circ$  (the parameters of figure 4), i.e. there appear to be two solutions of the saddle-point conditions. However, there is not a second region of absolute instability because although the points on the dashed line are branch points they are not pinch points. For example, figures 6(a) and 6(b) show a pinch point and a branch point,

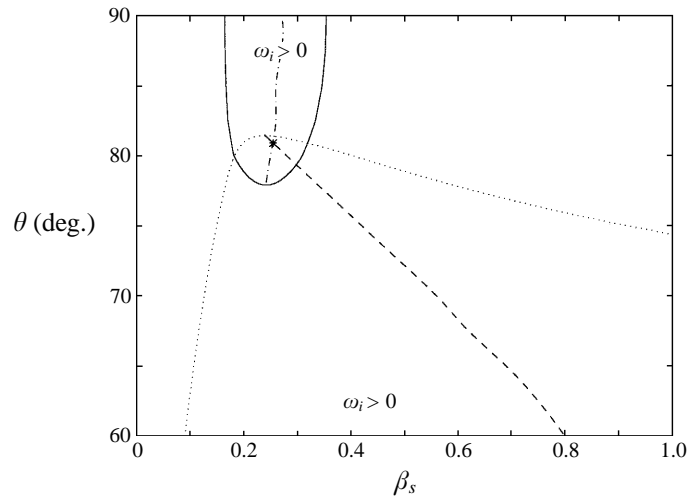


FIGURE 5. Lines where  $\omega_i = \partial\omega/\partial\alpha_c = 0$  (— and  $\cdots$ ) and lines where  $\partial\omega/\partial\alpha_c = \partial\omega_i/\partial\beta_{sr} = 0$  ( $-\cdot-$  and  $----$ ) for  $R_s = 1000$  and  $\beta_H = -0.1$ . The asterisk marks  $\beta_s \approx 0.255$  and  $\theta \approx 80.9^\circ$ , which are the parameters relevant to figures 4 and 6.

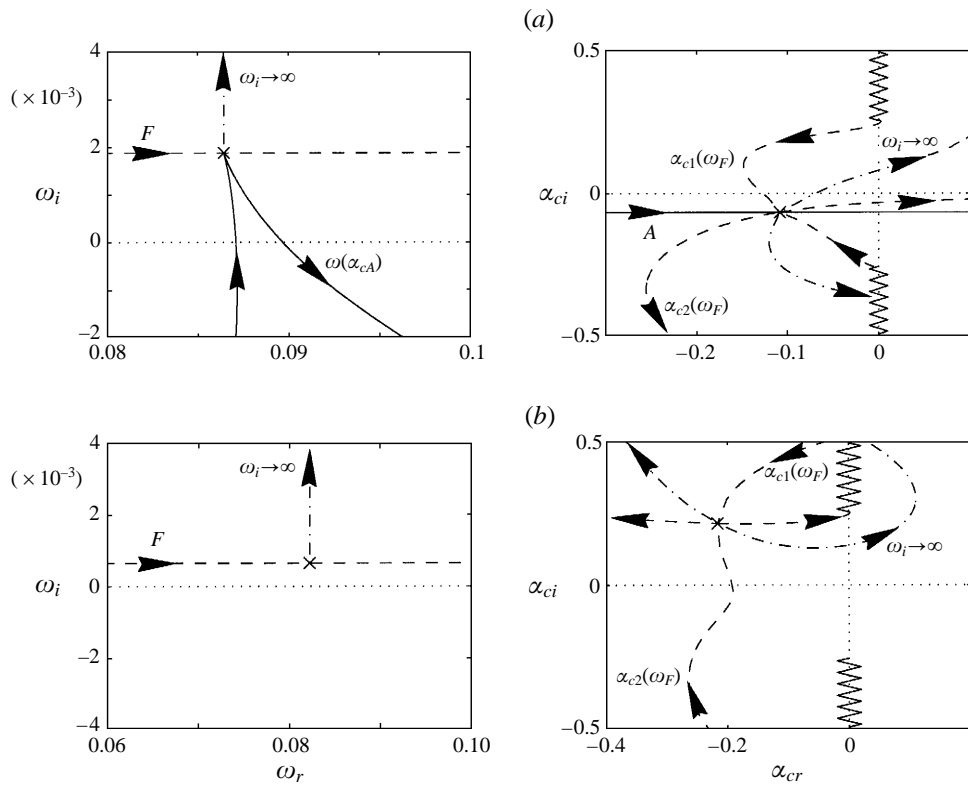


FIGURE 6. (a) Same pinch point as shown in figure 4 (a). (b) Second branch point ( $\times$ ) and the associated spatial branches in the  $\alpha_c$ -plane (given by the  $F$ -contour) for  $\beta_H = -0.1$ ,  $\theta \approx 80.9^\circ$  and  $\beta_s \approx 0.255$ .

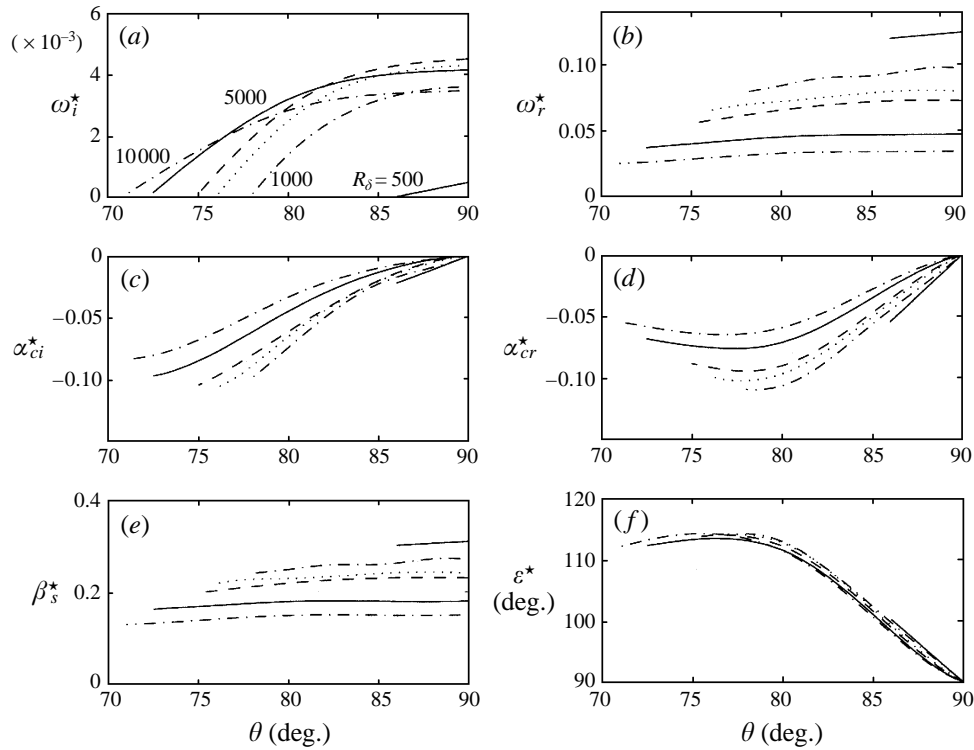


FIGURE 7. Reynolds-number and  $\theta$  dependences of components with maximum chordwise absolute instability for ranges of  $\theta$  with  $\omega_i^* \geq 0$  and  $\beta_H = -0.1$ . For all points  $\beta_{si}^* = \partial\omega_i/\partial\beta_{sr}|_{\alpha^*,\beta^*} = \partial\omega/\partial\alpha_c|_{\alpha^*,\beta^*} = 0$ . —,  $R_\delta = 500$ ; - · - ·,  $R_\delta = 1000$ ; · · · ·,  $R_\delta = 1500$ ; - - - -,  $R_\delta = 2000$ ; —,  $R_\delta = 5000$ ; - · - ·,  $R_\delta = 10000$ .

respectively, at the parameters marked by the asterisk in figure 5, i.e.  $\beta_H = -0.1$ ,  $\theta \approx 80.9^\circ$  and  $\beta_s \approx 0.255$ . The dashed-dotted lines in figure 6(b) show that both the spatial branches originate in the upper-half  $\alpha_c$ -plane. The  $F$ -contour is pictured passing through the branch point and mapping to two spatial branches in the  $\alpha_c$ -plane, but because there is no pinching there is no reason why the  $F$ -contour could not be lowered to the real  $\omega$ -axis while simultaneously deforming the  $A$ -contour (following Briggs' method) giving a purely convectively unstable response to (2.14). Two coalescing spatial branches that originate in the same half  $\alpha_c$ -plane create a second-order pole. For such cases, there is a period of algebraic growth, which may be important if the second-order pole is near neutral, but ultimately the behaviour will be exponential and dictated by the sign of  $\alpha_{ci}$ .

The Reynolds-number and  $\theta$  dependences of the chordwise absolute instability for  $\beta_H = -0.1$  are shown in figure 7. For all points in figure 7  $U^*$ ,  $\beta_{si}^*$  and  $\partial\omega_i/\partial\beta_{sr}|_{\alpha^*,\beta^*}$  are zero, and the pinching requirements are satisfied. In (a)  $\omega_i^*$  (the magnitude of the maximum absolute growth rate) is shown to increase with  $\theta$  and the maximum value of  $\omega_i^*$  initially increases with  $R_\delta$  but then begins to decrease again for  $R_\delta > 2000$ . For the given Reynolds numbers,  $\omega_r^*$  (figure 7 b) is non-zero and positive throughout, and  $\alpha_{ci}^* \leq 0$  (see c), which means that the most absolutely unstable modes correspond to travelling disturbances that lie within the convectively unstable region for the downstream ( $x_c > 0$ ) propagating branch of the dispersion relation that coalesces at the pinch points. The other branch that coalesces at the pinch points corresponds

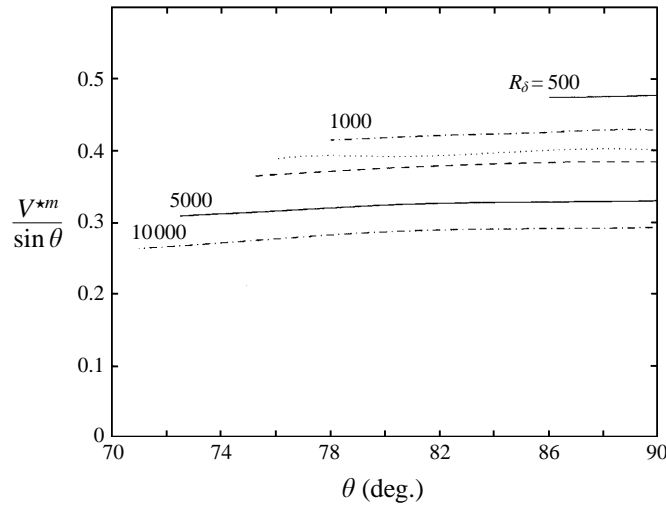


FIGURE 8. Variation in  $V^{*m}$  with Reynolds number and  $\theta$  for  $\beta_H = -0.1$ . —,  $R_\delta = 500$ ; - · - ·,  $R_\delta = 1000$ ; · · · · ·,  $R_\delta = 1500$ ; - - - -,  $R_\delta = 2000$ ; —,  $R_\delta = 5000$ ; - · - ·,  $R_\delta = 10000$ .

to a damped upstream ( $x_c < 0$ ) propagating mode. For  $\theta < 90^\circ$ ,  $\varepsilon^* = \tan^{-1}(\beta_s^*/\alpha_{cr}^*)$  (measured in the same way as  $\theta$  from the chordwise direction and shown in figure 7*f*) is always greater than  $90^\circ$ ;  $\alpha_{cr}^*$  is always negative (see *d*) for positive  $\beta_s^*$  (see *e*). The wave fronts are inclined at between  $0^\circ$  and about  $25^\circ$  to the chordwise direction. Interestingly, for a given  $\theta$  and  $\beta_H$ , the Reynolds-number dependence of  $\varepsilon^*$  is very weak with all the curves lying on top of one another. This suggests that the chordwise absolute instability is essentially an inviscid mechanism and may be related to the form of the mean velocity profiles in the  $\varepsilon^*$ -direction.

In figure 8,  $V^{*m}/\sin\theta$  is plotted. The reason for this scaling of  $V^{*m}$  is that  $V^{*m} = V^{*m*}/U_\infty^*$  (because  $U_\infty^*$  is the non-dimensionalizing velocity scale in this study), but choosing to plot the dimensional propagation velocity of the component with the maximum absolute growth rate as a proportion of the spanwise potential flow velocity gives  $V^{*m*}/V_{s\infty}^* = V^{*m}/\sin\theta$ . Like  $\beta_s^*$ ,  $V^{*m}/\sin\theta$  is insensitive to  $\theta$ , but decreases with increasing  $R_\delta$ .

For adverse pressure gradients, the flow angle only reaches  $90^\circ$  at infinite Reynolds number, so the results for  $\theta = 90^\circ$  in figure 7 are non-physical. However, for  $\theta < 90^\circ$ , it may be that in certain adverse-pressure-gradient flows the combination of flow angle and Reynolds number is such that there is a chordwise absolute instability. Free-stream-excited disturbances would then only convect in the spanwise direction, while growing in time at fixed chordwise positions.

### 3.2. The attachment-line flow

A boundary layer with  $\beta_H = m = 1.0$  and non-zero  $\theta$  will be discussed. This flow is the swept-Hiemenz problem that corresponds to a flow impinging on a yawed flat plate (i.e. a yawed  $180^\circ$  wedge). It also occurs on any swept blunt-nosed body at the attachment line. The two-dimensional stagnation flow was found to be stable to infinitesimally small disturbances propagating along  $y_s$  by Wilson & Gladwell (1978). The linear and nonlinear stability of the swept attachment-line flow has been studied by Hall, Malik & Poll (1984) and Spalart (1988), and the stability of this flow away from the attachment line has been studied by Spalart (1989) and Malik, Li & Chang (1991).

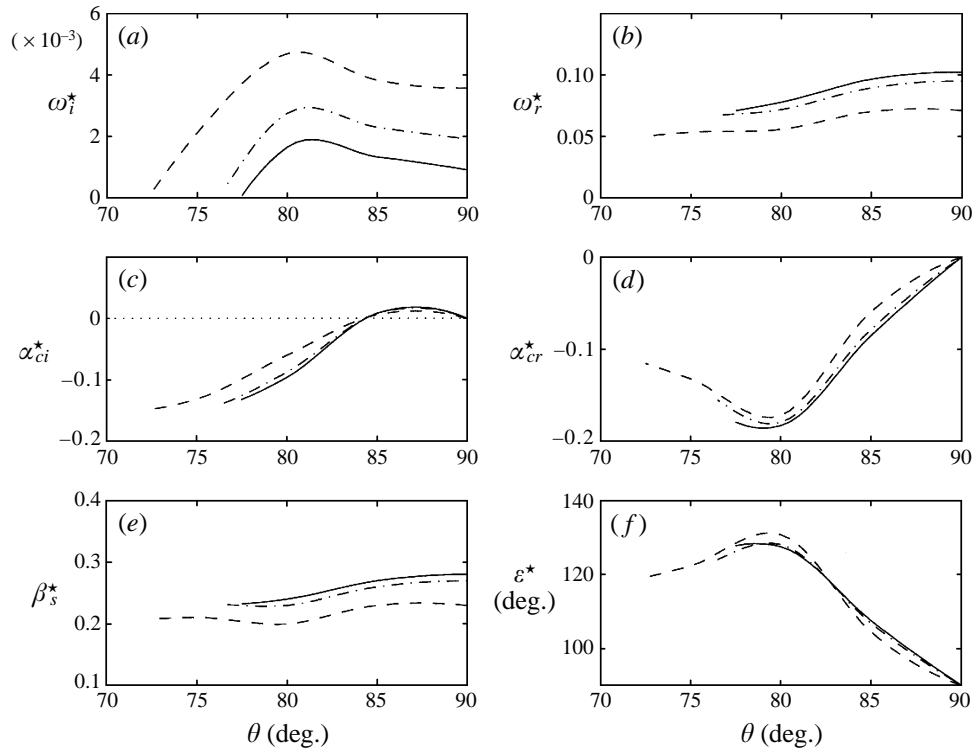


FIGURE 9. Reynolds-number and  $\theta$  dependences of components with maximum chordwise absolute instability for ranges of  $\theta$  with  $\omega_i^* \geq 0$  and  $\beta_H = 1.0$ . For all points  $\beta_{si}^* = \partial\omega_i/\partial\beta_{sr}|_{\alpha^*,\beta^*} = \partial\omega/\partial\alpha_c|_{\alpha^*,\beta^*} = 0$ . —,  $R_\delta = 800$ ; - · - ·,  $R_\delta = 1000$ ; ----,  $R_\delta = 2000$ .

Although on swept wings a pressure gradient of  $\beta_H = 1.0$  can only occur at the attachment line, where the flow is purely in the spanwise direction, the results presented by Mack (1984) suggest that all flows with strong favourable pressure gradients will have similar characteristics. The range within which  $\beta_H = 1.0$  is a good approximation to the flow around the leading edge of a swept wing depends on the cross-sectional shape of the aerofoil and the Reynolds number; the error increases as the radius of curvature of the leading edge decreases. On the attachment line, where  $\theta = 90^\circ$ ,  $\delta \approx 1.026$ , the non-dimensional boundary-layer thickness (defined as the height at which the velocity has reached 99% of the free-stream value) is about 3.055 and the non-dimensional momentum thickness is about 0.404. In fact, on the attachment line  $l^* = (v^*/C^*)^{1/2}$  is constant, as is  $\delta^*$ ,  $U_\infty^* = V_{s\infty}^*$  and  $R_\delta = R_s$ .

Figure 9 is equivalent to figure 7, but here is for  $\beta_H = 1.0$ ;  $\beta_{si}^* = \partial\omega_i/\partial\beta_{sr} = \partial\omega/\partial\alpha_c = 0$  and the pinching requirements are satisfied. Lines of  $\omega_i^* \geq 0$  are given in figure 9(a), which shows that the maximum absolute growth rate increases with  $R_\delta$  and, for fixed  $R_\delta$ , peaks at a value of  $\theta$  close to  $80^\circ$ . Figure 9(b) shows  $\omega_r^*$ , which is positive throughout, i.e. the components with chordwise absolute instability are travelling waves. On the attachment line itself (where  $\theta = 90^\circ$  and  $\beta_H = 1.0$ )  $\alpha_c^*$  (see c and d) was found to be zero, which means that these waves with chordwise absolute instability are equivalently two-dimensional waves with wave fronts that are normal to the leading edge convecting purely in the spanwise direction with a maximum temporal growth rate given by  $\omega_i^*$  travelling at  $V^{*m}$ . This is consistent with Poll's (1984) observations of free-stream-excited wave packets that convect in the spanwise

direction along the attachment line of swept cylinders (for  $R_s > 570$ ). These wave packets were observed to have wave fronts aligned normal to the leading edge. The breakdown to turbulence of these packets is via convective instability in the spanwise direction, i.e. linear growth of the disturbances as they are convected along the span leading to amplitudes sufficiently large to promote nonlinear behaviour and transition. These disturbances are amenable to  $e^n$ -method calculations in the spanwise direction; see Poll (1984). The critical Reynolds number for the onset of chordwise absolute instability on the attachment line is  $R_s = R_\delta \approx 681$ , which occurs for  $\beta_s^* \approx 0.29$  and  $\omega_r^* \approx 0.109$ . The overall critical spanwise Reynolds number for the onset of chordwise absolute instability for  $\beta_H = 1.0$  is  $R_s \approx 545$  ( $R_\delta = 561$ ), where  $\beta_s^* \approx 0.25$ ,  $\omega_r^* \approx 0.089$  and  $\theta \approx 82.1^\circ$ . For  $\theta < 90^\circ$ ,  $\alpha_{ci}^*$  first becomes positive and then becomes negative with decreasing  $\theta$ . This means that for  $\theta$  less than about  $85^\circ$  the spatial branch that originates in the upper-half  $\alpha_c$ -plane, and therefore gives a response in the region  $x_c - x_{c0} > 0$ , has crossed the real axis in order to reach the pinch point. This indicates that the absolutely unstable region lies within a region of convective instability for the downstream mode. The spatial branch that originates in the lower-half  $\alpha_c$ -plane does not cross the real axis and therefore it remains convectively stable in the region  $x_c - x_{c0} < 0$ . For  $\theta$  between about  $85^\circ$  and  $90^\circ$  the reverse is true: the absolute instability lies within a region of weak convective instability for the upstream mode and the spatial branch that originates in the upper-half  $\alpha_c$ -plane does not cross the real axis, remaining convectively stable in the region  $x_c - x_{c0} > 0$ . Figure 9(e) shows that  $\beta_s^*$  decreases with increasing  $R_\delta$ . The wave angle  $\varepsilon^* = \tan^{-1}(\beta_s^*/\alpha_{cr}^*)$  is plotted in figure 9(f) and (for  $\theta < 90^\circ$ ) it is always greater than  $90^\circ$ ;  $\alpha_{cr}^*$  (see d) is always negative for positive  $\beta_s^*$ . The wave fronts have a maximum inclination to the chordwise direction of about  $40^\circ$  at  $\theta \approx 80^\circ$ . The Reynolds-number and  $\theta$  dependences of  $V^{*m}$  for  $\beta_H = 1.0$  are similar to those for  $\beta_H = -0.1$  shown in figure 8.

#### 4. Conclusions

The disturbances on a family of three-dimensional boundary-layer flows have been investigated using linear stability theory. Motivated by the recent discovery of an absolute instability of the rotating-disk boundary layer (Lingwood 1995, 1996), this investigation has focused on the possibility of a similar mechanism operating in the swept-wing boundary layer. For attachment-line flows that are not prematurely tripped into a turbulent state by large-amplitude disturbances, it has been found that close to the attachment line there is a chordwise absolute instability above a critical spanwise Reynolds number of  $R_s \approx 545$  (occurring at  $\theta \approx 82.1^\circ$  and  $\beta_s \approx 0.25$ ). The critical Reynolds number for the onset of chordwise absolute instability on the attachment line itself, i.e. for  $\theta = 90^\circ$  and  $\beta_H = 1.0$ , is  $R_s = R_\delta \approx 681$ . It has been shown that there is chordwise absolute instability at large flow angles for an adverse-pressure-gradient flow ( $\beta_H = -0.1$ ). It is expected that the behaviour of Falkner–Skan–Cooke boundary layers with values of  $\beta_H$  other than 1.0 and  $-0.1$  will be similar.

The chordwise absolute instability does not prevent disturbances convecting in the spanwise direction. Furthermore, the absolute instability mechanism does not predict how far along the span the disturbances are convected before the onset of transition but, provided the spanwise extent of the flow is large enough for critical disturbance amplitudes to be reached before being convected out of the domain of interest (e.g. beyond the end of the wing), it is possible that the onset of absolute instability indicates the chordwise position of the onset of nonlinearity, which may lead to

transition to turbulence. Alternatively, because the chordwise absolute instability at the attachment line inhibits the propagation of disturbances into the rest of the flow, it may be that disturbances are swept along the span without causing transition and without contaminating the rest of the flow. If this suggestion is the case it would imply that the chordwise absolute instability helps to keep the flow laminar by limiting the propagation of disturbances that enter the boundary layer at the attachment line. At the very least these results give useful information on the propagation of wave packets in laminar swept boundary-layer flows, and allay the speculation about absolute instability of swept-wing boundary layers arising from the suggestive results for the rotating-disk boundary layer.

This work was performed while supported by a Research Fellowship at Pembroke College, Cambridge, and has benefited from discussions with Dr J. J. Healey.

## REFERENCES

- ASHPIS, D. E. & RESHOTKO, E. 1990 The vibrating ribbon problem revisited. *J. Fluid Mech.* **213**, 531–547.
- BERS, A. 1975 Linear waves and instabilities. In *Physique des Plasmas* (ed. C. DeWitt & J. Peyraud), pp. 117–215. Gordon & Breach.
- BREUDO, L. 1991 Three-dimensional absolute and convective instabilities, and spatially amplifying waves in parallel shear flows. *Z. Angew. Math. Phys.* **42**, 911–942.
- BRIGGS, R. J. 1964 *Electron-Stream Interaction with Plasmas*, chap. 2. MIT Press.
- COOKE, J. C. 1950 The boundary layer of a class of infinite yawed cylinders. *Proc. Camb. Phil. Soc.* **46**, 645–648.
- GASTER, M. 1967 On the flow along swept leading edges. *Aero. Q.* **18**, 165–184.
- GRAY, W. E. 1952 The nature of the boundary layer at the nose of a swept back wing. *Unpublished, Min. Aviation, Lond.*
- GREGORY, N., STUART, J. T. & WALKER, W. S. 1955 On the stability of three-dimensional boundary layers with application to the flow due to a rotating disk. *Phil. Trans. R. Soc. Lond. A* **248**, 155–199.
- HALL, P., MALIK, M. R. & POLL, D. I. A. 1984 On the stability of an infinite swept attachment line boundary layer. *Proc. R. Soc. Lond. A* **395**, 229–245.
- HUERRE, P. & MONKEWITZ, P. A. 1990 Local and global instabilities in spatially developing flows. *Ann. Rev. Fluid Mech.* **22**, 473–537.
- KUPFER, K., BERS, A. & RAM, A. K. 1987 The cusp map in the complex-frequency plane for absolute instabilities. *Phys. Fluids* **30**, 3075–3082.
- LINGWOOD, R. J. 1995 Absolute instability of the boundary layer on a rotating disk. *J. Fluid Mech.* **299**, 17–33.
- LINGWOOD, R. J. 1996 An experimental study of absolute instability of the rotating-disk boundary-layer flow. *J. Fluid Mech.* **314**, 373–405.
- LINGWOOD, R. J. 1997a On the effects of suction and injection on the absolute instability of the rotating-disk boundary layer. *Phys. Fluids* **9**, 1317–1328.
- LINGWOOD, R. J. 1997b Absolute instability of the Ekman layer and related rotating flows. *J. Fluid Mech.* **331**, 405–428.
- LINGWOOD, R. J. 1997c On the application of the Briggs' and steepest-descent methods to a boundary-layer flow. *Stud. Appl. Maths* **98**, 213–254.
- MACK, L. M. 1984 Boundary-layer stability theory. In *AGARD Rep.* 709, pp. 3-1–3-81.
- MALIK, M. R., LI, F. & CHANG, C.-L. 1991 Crossflow disturbances in three-dimensional boundary layers: nonlinear development, wave interaction and secondary instability. *J. Fluid Mech.* **268**, 1–36.
- MÜLLER, B. & BIPPES, H. 1988 Experimental study of instability modes in a three-dimensional boundary layer. In *AGARD Conf. Proc.* 438, pp. 13-1–13-13.
- POLL, D. I. A. 1979 Transition in the infinite swept attachment-line boundary layer. *Aero. Q.* **30**, 607–628.

- POLL, D. I. A. 1984 Transition description and prediction in three-dimensional flows. In *AGARD Rep.* 709, pp. 5-1-5-23.
- POLL, D. I. A. 1985 Some observations of the transition process on the windward face of a long yawed cylinder *J. Fluid Mech.* **150**, 329-356.
- PFENNINGER, W. 1977 Laminar flow control, laminarization. *Paper 3, Special Course on Concepts for Drag Reduction, AGARD Rep.* 654.
- ROSENHEAD, L. 1963 *Laminar Boundary Layers*, First Edn, pp. 470-471. Oxford University Press.
- SPALART, P. R. 1988 Direct numerical study of leading-edge contamination. In *AGARD Conf. Proc.* 438, pp. 5-1-5-13.
- SPALART, P. R. 1989 Direct numerical study of crossflow instability. In *Laminar-Turbulent Transition* (ed. D. Arnal & R. Michel), pp. 622-630.
- SQUIRE, H. B. 1933 On the stability for three-dimensional disturbances of viscous fluid flow between parallel walls. *Proc. R. Soc. Lond. A* **142**, 621-628.
- WILSON, S. D. R. & GLADWELL, I. 1978 The stability of a two-dimensional stagnation flow to three-dimensional disturbances. *J. Fluid Mech.* **84**, 517-528.